

Thermo-molecular gas-film lubrication dynamics considering boundary temperature and ambient gas (2-DOF numerical analysis by t-MGL equation)

Shigehisa Fukui¹ · Yuki Okamura¹ · Atsushi Nakasuji¹ · Hiroshige Matsuoka¹

Received: 18 September 2015 / Accepted: 31 December 2015 / Published online: 9 January 2016
© Springer-Verlag Berlin Heidelberg 2016

Abstract The static and dynamic flying characteristics of a slider in a hard disk drive have become an important consideration owing to recent increases in recording density. In the present paper, the characteristics of a plane inclined slider (Case 1) and a step slider flying in either air or He (Case 2) over a running boundary wall with local temperature distributions are analyzed using the thermo-molecular gas-film lubrication (t-MGL) equation. For a plane inclined slider (Case 1), the fundamental static and dynamic characteristics are analyzed numerically and are examined through two limiting approximations: the approximation for infinite bearing number and the incompressible short bearing approximation. For a step slider (Case 2), the decreases in the minimum spacing for a slider flying in He are significant because the mean free path of He, λ_{He} , is approximately three times that of air, λ_{air} . The increases in the minimum spacing due to laser heating are negligible in both air and He because the heat spot size is very small. Moreover, the decrease in the minimum spacing produced by thermal deformation (projection height, d_{max}) by laser heating in the thermal fly-height control slider is reduced by the total additional pressure of (1) MGL pressures produced by the air-film wedge effect, (2) t-MGL pressures produced by the applied temperature distribution, and (3) van der Waals attractive pressure due to the ultra-small spacing. The spacing fluctuation in He caused by a running wavy disk is smaller than that in air, because the inlet-to-outlet spacing ratio (h_1/h_0) in He is larger than that in air.

1 Introduction

Thermal fly-height control (TFC) and heat-assisted magnetic recording (HAMR) have been proposed as new magnetic recording techniques in order to increase the recording density of hard disk drives (HDDs) (Kurita et al. 2005; Peng et al. 2005; Dahl and Bogy 2014). In addition, He-enclosed HDDs can significantly reduce windage loss, disk flutter, and temperature increase, because He has a lower density and a higher heat conductivity than air (Ohkubo et al. 1989; Liu et al. 2011; Fukui et al. 2014a, b).

In the present paper, using the thermo-molecular gas-film lubrication (t-MGL) equation, we first examine the static and dynamic air-film characteristics of a plane inclined slider by a heat spot (Case 1), and then a step slider flying in either air or He over a running boundary wall with local temperature distributions and thermal deformation (projection) (Case 2) are analyzed. The aims of Cases 1 and 2 are to understand the physics of pressure generation produced by boundary temperature (Case 1) and to examine more realistic flying characteristics in modern HDD (Case 2), respectively. In this paper, the heat transfer at the interface is neglected.

2 Fundamental equations

2.1 Equations of motion

The equations of motion for a slider with two DOF are expressed as:

$$m\ddot{z} + kz = \int_0^b \int_0^l \Delta p dx dy, \quad (1)$$

✉ Shigehisa Fukui
fukui@damp.tottori-u.ac.jp

¹ Department of Mechanical and Aerospace Engineering,
Tottori University, 4-101, Minami, Koyama,
Tottori 680-8552, Japan

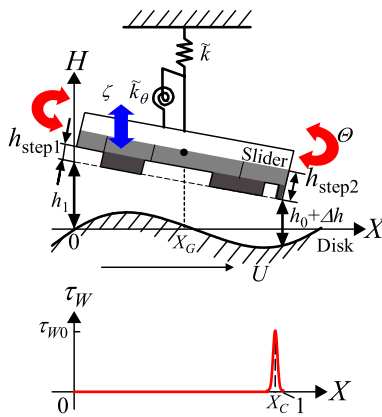


Fig. 1 Two-DOF model slider with local boundary temperature distribution

$$J\ddot{\theta} + k_{\theta}\theta = \int_0^b \int_0^l \Delta p \cdot (x_G - x) dx dy, \quad (2)$$

where z and θ are the translational and pitching displacements, respectively, m and J are the mass and the moment of inertia for pitching motion, respectively, l and b are the slider's length and width, respectively, k and k_{θ} are the translational and pitching stiffnesses of the suspension, respectively, and Δp is the dynamic pressure, as shown in Fig. 1.

2.2 Thermo-molecular gas-film lubrication (t-MGL) equation

The thermo-molecular gas-film lubrication (t-MGL) equation with time-dependence to examine dynamic characteristics is given by (Fukui et al. 2001, 2014a, b):

$$\begin{aligned} & \left(\frac{b}{l}\right)^2 \frac{\partial}{\partial X} \left\{ \tilde{Q}_p(D) \frac{PH^3}{1 + \tau_w} \frac{\partial P}{\partial X} - \tilde{Q}_T(D) \frac{P^2 H^3}{(1 + \tau_w)^2} \frac{\partial \tau_w}{\partial X} \right\} \\ & + \frac{\partial}{\partial Y} \left\{ \tilde{Q}_p(D) \frac{PH^3}{1 + \tau_w} \frac{\partial P}{\partial Y} - \tilde{Q}_T(D) \frac{P^2 H^3}{(1 + \tau_w)^2} \frac{\partial \tau_w}{\partial Y} \right\} \\ & = \Lambda_b \frac{\partial}{\partial X} \left(\frac{PH}{1 + \tau_w} \right) + \sigma_b \frac{\partial}{\partial \tilde{t}} \left(\frac{PH}{1 + \tau_w} \right), \end{aligned} \quad (3)$$

where P ($=p/p_a$, p_a ambient pressure) is the non-dimensional pressure, H ($=h/h_0$, h_0 minimum spacing) is the non-dimensional spacing, \tilde{t} ($=\omega_0 t$, ω_0 normalizing angular frequency) is the non-dimensional time, X ($=x/l$) and Y ($=y/b$) are non-dimensional coordinates, D is the inverse Knudsen number defined as $D = ph/\mu\sqrt{2RT}$, Λ_b ($\equiv 6\mu Ub^2/p_a h_0^2 l$) is the bearing number, and σ_b ($\equiv 12\mu\omega_0 b^2/p_a h_0^2$) is the squeeze number. The quantities $\tilde{Q}_p(D)$ ($\equiv Q_p/Q_{pcon}$) and $\tilde{Q}_T(D)$ ($\equiv Q_T/Q_{Tcon}$) are the pressure flow rate ratio and the thermal creep flow rate ratio, respectively. The relationships between Q_p and D and between Q_T and D when

accommodation coefficients of the slider, α_s , and the disk, α_d , are both unity ($\alpha_s = \alpha_d = 1$), that is, molecules reflect diffusely at boundaries, are presented by means of a database in references (Fukui and Kaneko 1990b; Fukui et al. 2014a, b). The non-dimensional temperature $\tau_w (=T/T_0 - 1)$ in Eq. (3) is defined as the average temperature of the slider surface, τ_{ws} , and the disk surface, τ_{wd} , i.e., $\tau_w = (\tau_{ws} + \tau_{wd})/2$.

For a different gas, such as helium, the pressure generation can be obtained by solving Eq. (3) using the same database of Q_p and Q_T values and the corresponding values of viscosity μ and the gas constant R . The mean free path values used in the calculations are $\lambda_{air} = 64$ nm for air and $\lambda_{He} = 190$ nm for He, whereas the viscosity values are 1.81×10^{-5} Pa s for air and 1.96×10^{-5} Pa s for He. The gas constants R are 287.03 J/(kg K) for air and 2077.15 J/(kg K) for He.

2.3 Thermal creep flow

When the Knudsen number, K_n , is not negligible (or when the molecular mean free path is not negligible compared with the spacing) and temperature gradients exist along the boundary walls, a special type of flow, referred to as thermal creep flow or thermal transpiration flow, is induced from the colder regions to the hotter regions. When the boundary temperature has a symmetric distribution, levitation pressure (force) occurs under the slider (Fukui and Kaneko 1988; Fukui et al. 2001).

Pressure generated by the thermal creep flow is evident when the boundary is stationary or moves very slowly, because the wedge effect is insignificant (Fukui et al. 2014a). In contrast, when the boundary (disk) is running, pressures generated by the wedge effect overwhelm those generated by the thermal creep flow (Fukui et al. 2014b). Therefore, in the latter part of the present study (Case 2), we neglect the thermal creep flow terms:

$$\begin{aligned} & \left(\frac{b}{l}\right)^2 \frac{\partial}{\partial X} \left\{ \tilde{Q}_p(D) \frac{PH^3}{1 + \tau_w} \frac{\partial P}{\partial X} \right\} + \frac{\partial}{\partial Y} \left\{ \tilde{Q}_p(D) \frac{PH^3}{1 + \tau_w} \frac{\partial P}{\partial Y} \right\} \\ & = \Lambda_b \frac{\partial}{\partial X} \left(\frac{PH}{1 + \tau_w} \right) + \sigma_b \frac{\partial}{\partial \tilde{t}} \left(\frac{PH}{1 + \tau_w} \right). \end{aligned} \quad (4)$$

2.4 Van der Waals (vdW) force equation

The vdW pressure P_{vdW} between the slider and the disk is expressed as (Israelachvili 1992; Matsuoka et al. 2005):

$$P_{vdW} = -\tilde{A}_{132} / 6\pi H^3, \quad (5)$$

where \tilde{A}_{132} ($=A_{132}/p_a h_0^3$) is the non-dimensional Hamaker constant determined from the refractive indices of the solids. When both the disk and the slider have diamond-like

carbon (DLC) coatings, A_{132} will be 3.26×10^{-19} J. From this equation, we obtain the static force (attractive pressure) and dynamic pressure (negative stiffness).

3 Analysis method

3.1 Perturbation method

In order to analyze the static and dynamic slider characteristics, we used the perturbation method while assuming that the spacing fluctuation Δh is small compared with the minimum spacing h_0 . We obtained the following equation for the static pressure P_0 and the infinitesimal dynamic pressure $\psi (= \Delta p/p_a)$:

$$P(X, Y, \tilde{t}) = P_0(X, Y) + \psi(X, Y, \tilde{t}), \quad \psi \ll P_0. \quad (6)$$

The spacing between the slider and the disk, H , consists of the time-independent spacing, H_0 , and time-dependent infinitesimal variations, $\eta (= \Delta h/h_0)$:

$$H(X, Y, \tilde{t}) = H_0(X, Y) + \eta(X, Y, \tilde{t}), \quad \eta \ll H_0. \quad (7)$$

By substituting Eqs. (6) and (7) into Eqs. (3) (or Eq. (4)) and (5), we obtain the static equilibrium equation and the linearized dynamic equation.

3.2 Fundamental equation giving dynamic pressure ψ

In order to obtain a simple relationship between σ_b and Λ_b , the characteristic frequencies are determined to be

$$f_L \equiv U/l \quad \text{and} \quad \omega_0 = 2\pi f_L, \quad (8)$$

where U is the disk speed.

This frequency (f_L) is the frequency that gives the geometric restriction of the spacing fluctuation caused by a running wavy wall. The non-dimensional frequency Ω is given by

$$\Omega = \omega/\omega_0 = f/f_L. \quad (9)$$

The relationship between σ_b and Λ_b , from their definitions and Eq. (9), is expressed as

$$\begin{aligned} \sigma_b &= \Lambda_b (2l\omega_0/U) \\ &= 4\pi \Lambda_b. \end{aligned} \quad (10)$$

For a wavy mode, Ω is equivalent to the slider ratio, R_S , which is the ratio of the slider length, l , to the wavelength of a wavy wall, L , i.e.:

$$\Omega = f/f_L = l/L \equiv R_S. \quad (11)$$

The small spacing fluctuation η in Eq. (7) consists of the translational and pitching displacements of the slider, $\zeta(=z/h_0)$, $\Theta(=\theta/h_0)$, and the displacement of the disk surface ζ_d :

$$\eta = \zeta + \Theta \cdot (X_G - X) - \zeta_d, \quad (12)$$

where the disk displacements for a wavy mode are as follows:

$$\zeta_d = \tilde{a} \sin(2\pi \Omega X - \Omega \tilde{t}). \quad (13)$$

Therefore, the dynamic pressure can be divided into components of each displacement and is given by:

$$\psi = G_1(X, Y) \cdot \zeta(\tilde{t}) + G_2(X, Y) \cdot \Theta(\tilde{t}) + G_3(X, Y) \cdot \tilde{a} \sin(\Omega \tilde{t}), \quad (14)$$

where G_k ($k = 1-3$) are the dynamic pressure coefficients generated by the translational displacement, the pitching displacement, and the displacement of the disk surface, respectively. We performed numerical analysis using the finite volume method for a two-dimensional linear differential equation, which gives the dynamic pressure coefficient G_k , in the frequency domain (Ono 1975).

Substituting Eq. (14) into Eqs. (1) and (2), the equations of motion are expressed as:

$$\begin{aligned} \tilde{m}\ddot{\zeta} + \gamma_{11}\dot{\zeta} + \gamma_{12}\dot{\Theta} + (\kappa_{11} + \tilde{k})\zeta + \kappa_{12}\Theta \\ = \tilde{a} (\delta_{s1} \cdot \sin \Omega \tilde{t} + \delta_{c1} \cdot \cos \Omega \tilde{t}) \end{aligned} \quad (15)$$

and

$$\begin{aligned} \tilde{J}\ddot{\Theta} + \gamma_{21}\dot{\zeta} + \gamma_{22}\dot{\Theta} + \kappa_{21}\zeta + (\kappa_{22} + \tilde{k}_\theta)\Theta \\ = \tilde{a} (\delta_{s2} \cdot \sin \Omega \tilde{t} + \delta_{c2} \cdot \cos \Omega \tilde{t}), \end{aligned} \quad (16)$$

where κ_{ij} and γ_{ij} ($i = 1, 2, j = 1, 2$) are the stiffnesses and damping coefficients obtained from G_1 and G_2 , respectively (Fukui et al. 1985).

The real and imaginary parts of quantities $-G_1$ and $-G_2 \cdot (X_G - X)$ are the stiffnesses and damping coefficients for translational and pitching motions, respectively.

4 Two approximate solutions for limiting cases

4.1 Static and dynamic approximate solutions for an infinite bearing number ($\Lambda_b \rightarrow \infty$)

For a spacing of several nanometers, the conventional bearing number Λ , and, therefore, Λ_b and σ_b also increase dramatically (see Eq. (10)). For an infinite bearing number, Eq. (3) is expressed as

$$\frac{\partial}{\partial X} \left(\frac{PH}{1 + \tau_W} \right) + 4\pi \frac{\partial}{\partial \tilde{t}} \left(\frac{PH}{1 + \tau_W} \right) = 0. \quad (17)$$

Note that in Eq. (17) for $\Lambda_b \rightarrow \infty$, the temperature distribution τ_W is arbitrary.

The static solution of Eq. (17) is as follows:

$$P_0|_{\Lambda_b \rightarrow \infty} = (1 + \tau_W) \cdot P_0|_{\Lambda_b \rightarrow \infty, \tau_W=0} \quad (18)$$

where

$$P_0|_{\Lambda_b \rightarrow \infty} = H'_1/H_0 \quad (H'_1 \text{ is the inlet spacing}) \quad (19)$$

The quantity $P_0|_{\Lambda_b \rightarrow \infty}$ is the conventional approximation solution for an infinite bearing number without a local temperature distribution (Fukui and Kaneko 1990a).

The dynamic solutions for Eq. (17) are as follows:

$$G_k|_{\Lambda_b \rightarrow \infty} = (1 + \tau_W) \cdot G_k|_{\Lambda_b \rightarrow \infty, \tau_W=0}, \quad k = 1, 2, 3 \quad (20)$$

where

$$\begin{aligned} G_1|_{\Lambda_b \rightarrow \infty} &= \frac{1}{H_0} \left\{ \cos(4\pi \Omega X) - \frac{H_1}{H_0} \right\} - i \frac{1}{H_0} \sin(4\pi \Omega X), \\ G_2|_{\Lambda_b \rightarrow \infty} &= \frac{1}{H_0} \left\{ X_G \cos(4\pi \Omega X) - \frac{H_1}{H_0} (X_G - X) \right\} \\ &\quad - i \frac{X_G}{H_0} \sin(4\pi \Omega X), \\ G_3|_{\Lambda_b \rightarrow \infty} &= \frac{1}{H_0} \left\{ \cos(4\pi \Omega X) - \frac{H_1}{H_0} \cos(2\pi \Omega X) \right\} \\ &\quad - i \frac{1}{H_0} \left\{ \sin(4\pi \Omega X) - \frac{H_1}{H_0} \sin(2\pi \Omega X) \right\}. \end{aligned} \quad (21)$$

The quantities $G_k|_{\Lambda_b \rightarrow \infty}$ ($k = 1-3$) shown in Eq. (21) are also conventional approximation solutions for an infinite bearing number without a local temperature distribution (Fukui and Kaneko 1990a).

The static and dynamic pressure increases produced by the boundary temperature for $\Lambda_b \rightarrow \infty$ are as follows:

$$\begin{aligned} \delta P_0|_{\Lambda_b \rightarrow \infty} &\equiv P_0|_{\Lambda_b \rightarrow \infty, \tau_W} - P_0|_{\Lambda_b \rightarrow \infty, \tau_W=0} \\ &= \tau_W(X, Y) \cdot P_0|_{\Lambda_b \rightarrow \infty, \tau_W=0} \end{aligned} \quad (22)$$

$$\begin{aligned} \delta G_k|_{\Lambda_b \rightarrow \infty} &\equiv G_k|_{\Lambda_b \rightarrow \infty, \tau_W} - P_0 G_k|_{\Lambda_b \rightarrow \infty, \tau_W=0} \\ &= \tau_W(X, Y) \cdot G_k|_{\Lambda_b \rightarrow \infty, \tau_W=0} \quad (k = 1-3). \end{aligned} \quad (23)$$

These static and dynamic pressure increases can be the theoretical maximum values produced by the applied temperature.

4.2 Static and dynamic solutions by incompressible short bearing approximation ($\Lambda_b \rightarrow 0$)

This approximation is based on the assumptions that:

1. The slider width b is much smaller than slider length l : $b/l \ll 1$.

2. The bearing number is small: $\Lambda_b \ll 1$.
3. Neither the spacing H nor the applied temperature τ_W depend on Y :

$$H = H(X, \tilde{t}), \quad \tau_W = \tau_W(X).$$

Under these conditions, Eq. (3) is simplified to

$$\tilde{Q}_p \Big|_0 \frac{H^3}{1 + \tau_W} \frac{\partial^2 P}{\partial Y^2} = \Lambda_b \frac{\partial}{\partial X} \left(\frac{H}{1 + \tau_W} \right) + \sigma_b \frac{1}{1 + \tau_W} \frac{\partial H}{\partial \tilde{t}} \quad (24)$$

$$\text{where } \tilde{Q}_p \Big|_{D_0} = \tilde{Q}_p(D_0 H / \sqrt{1 + \tau_W}).$$

The static pressure, P_0 , is expressed as;

$$P_0 = \Lambda_b \cdot g_1 \cdot \frac{d}{dX} \left(\frac{H_0}{1 + \tau_W} \right) \cdot Y(Y - 1)/2 + 1. \quad (25)$$

Moreover, the complex dynamic component, G_k , is given by

$$\begin{aligned} G_k &= \Lambda_b \cdot \left\{ g_2 F_k + g_1 \frac{d}{dX} \left(\frac{F_k}{1 + \tau_W} \right) + i \cdot 4\pi \Omega g_1 \frac{F_k}{1 + \tau_W} \right\} \\ &\quad \cdot Y(Y - 1)/2, \quad (k = 1-3) \end{aligned} \quad (26)$$

where $\Omega = flf_0$ and

$$F_1 = 1, \quad F_2 = X_G - X, \quad F_3 = \cos(2\pi \Omega X) - i \cdot \sin(2\pi \Omega X)$$

$$g_1 = (1 + \tau_W) / \left\{ \tilde{Q}_p \Big|_{D_0 H_0} \cdot H_0^3 \right\}$$

$$\begin{aligned} g_2 &= -g_1^2 \left\{ \tilde{Q}_p \Big|_{D_0 H_0} \frac{3H_0^2}{1 + \tau_W} + \frac{D_0 H_0^3}{(1 + \tau_W)^{3/2}} \frac{\partial \tilde{Q}_p}{\partial D} \Big|_{D_0 H_0} \right\} \\ &\quad \cdot \frac{d}{dX} \left(\frac{H_0}{1 + \tau_W} \right). \end{aligned} \quad (27)$$

In the incompressible short bearing approximation, the stiffness κ_{ij} is independent of the frequency and the damping $\Omega \gamma_{ij}$ is proportional to the frequency.

5 Static and dynamic characteristics with local boundary temperature

5.1 Applied temperature

The temperature distributions at the slider or disk surface are considered to be Gaussian distributions, the maximum temperature of which is given by the parameter τ_{w0} , as follows:

$$\tau_W(X, Y) = \tau_{w0} \exp \left[-\frac{1}{2} \left\{ \left(\frac{X - X_C}{\sigma_x} \right)^2 + \left(\frac{Y - Y_C}{\sigma'_y} \right)^2 \right\} \right] \quad (28)$$

where σ_x and $\sigma'_y(=b/l) \cdot \sigma_y$ are the standard deviations and X_C and Y_C are the centers of the distribution in the x and y directions, respectively. The standard parameters in the temperature distribution are set to be $\sigma_x = \sigma'_y = 0.005$ and $X_C = 0.98, Y_C = 0.5$.

5.2 Fundamental characteristics for a plane inclined slider (Case 1)

We first examine the fundamental air-film characteristics by the heat spot for a plane inclined slider (see Fig. 2).

5.2.1 Static pressure generation in air produced by the heat spot

Figure 3 shows typical pressure distributions in an air atmosphere with a Gaussian heat spot near the trailing edge with a minimum spacing of $h_0 = 5$ nm, with a corresponding modified bearing number $\tilde{\Lambda}_b$ of 2.2×10^3 , and a slider inclination of $h_1/h_0 = 2$. A pressure spike can be observed near the trailing edge produced by the heat spot ($\tau_{w0} = 0.5$, which corresponds to a disk temperature increase of 300 K).

Figure 4a, b show the pressure distributions along the centerline ($Y = 0.5$) with the maximum temperature τ_{w0} as a parameter and minimum spacings of $h_0 = 5$ and 20 nm. Figure 4a shows a general view for $X = 0-1$, and Fig. 4b shows an enlarged view for $X = 0.9-1$. For a smaller spacing, say 1 or 2 nm, the pressure distributions approximately coincide to the approximate solutions for $\Lambda_b \rightarrow \infty$ (see Eq. (18)) corresponding to each maximum temperature τ_{w0} .

Figure 5a, b show pressure contour plots in an air atmosphere with a Gaussian heat spot near the trailing edge with minimum spacings of $h_0 = 5$ and 20 nm and the corresponding modified bearing numbers of $\Lambda_b = 2.2 \times 10^3$ and 705, respectively. The pressure profile for $h_0 = 5$ nm is greater and steeper than that for $h_0 = 20$ nm. Since the modified bearing number $\tilde{\Lambda}_b$ is very large for $h_0 = 5$ nm, the non-dimensional value of the pressure peak for $h_0 = 5$ nm is 0.88, which is close to the value of $\Delta P_{0HT} (=1)$, where ΔP_{0HT} denotes the theoretical maximum value of the additional pressure given by Eq. (A1) (see “Appendix 1”).

Figure 6 shows the relationships between the load carrying capacity, W , and the modified bearing number, $\tilde{\Lambda}_b(=\Lambda_b/\tilde{Q}_{P0})$, where \tilde{Q}_{P0} corresponds to the Poiseuille flow rate ratio for the minimum spacing, h_0 . For very large $\tilde{\Lambda}_b$, W is approximately constant and coincides with the approximate value for $\tilde{\Lambda}_b \rightarrow \infty$ (Eq. (18)). For $10^{-1} < \tilde{\Lambda}_b < 10^2$, W decreases and approximately coincide with the incompressible short bearing approximation ($\tilde{\Lambda}_b \rightarrow 0$, Eq. (25)), which is proportional to $\tilde{\Lambda}_b$. For $\tilde{\Lambda}_b < 10^{-1}$, numerical solutions approach constant values, whereas the short bearing approximation ($\tilde{\Lambda}_b \rightarrow 0$)

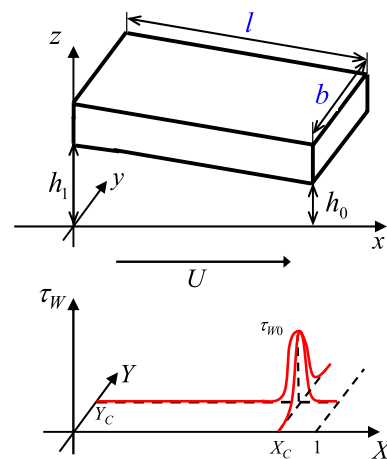


Fig. 2 Plane inclined slider with boundary temperature distribution (Case 1)

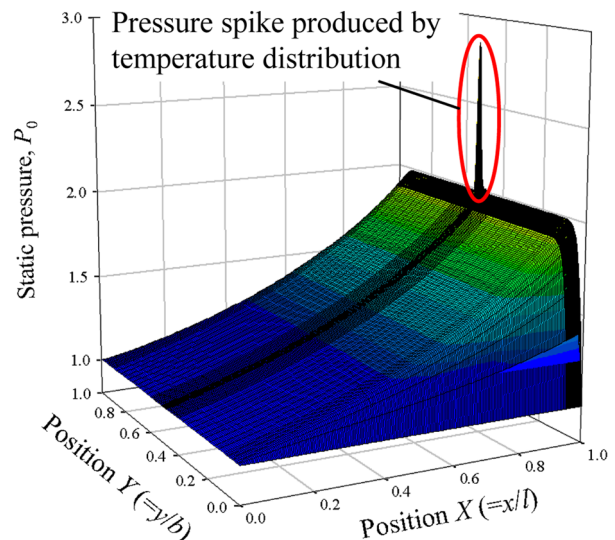


Fig. 3 Static pressure distributions with temperature distribution (in air). $h_0 = 5$ nm, $U = 10$ m/s ($\tilde{\Lambda}_b = 2.2 \times 10^3$), $h_1/h_0 = 2$, $h_{step1} = h_{step2} = 0$. $X_C = 0.98, Y_C = 0.5, \sigma_x = \sigma'_y = 0.005, l = b = 1$ m, $\tau_{w0} = 0.5$

continues to decrease. These differences between the numerical solutions and the short bearing approximation occur because numerical solutions that include the thermal creep flow term yield pressures produced by the thermal-wedge effect. (Fukui et al. 2014a). Note that in the short bearing approximation equation ($\tilde{\Lambda}_b \rightarrow 0$), the thermal creep flow term vanishes automatically.)

5.2.2 Dynamic pressure generation in air produced by the heat spot

Figure 7 shows the typical translational stiffness component $\{-Re(G_1)\}$ for the flying state of $\Omega = 1$ in an air

Fig. 4 Static pressure distributions for different spacings (in air). **a** General view ($X = 0-1$), **b** enlarged view ($X = 0.9-1$)

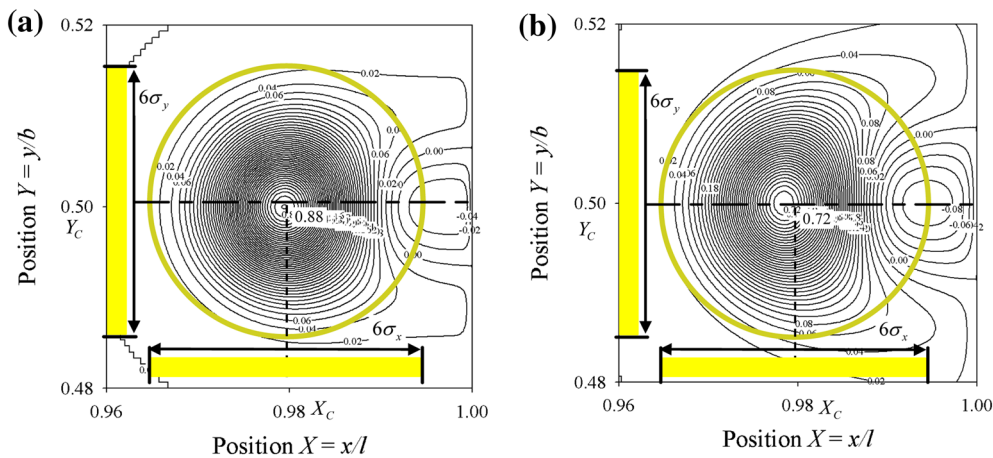
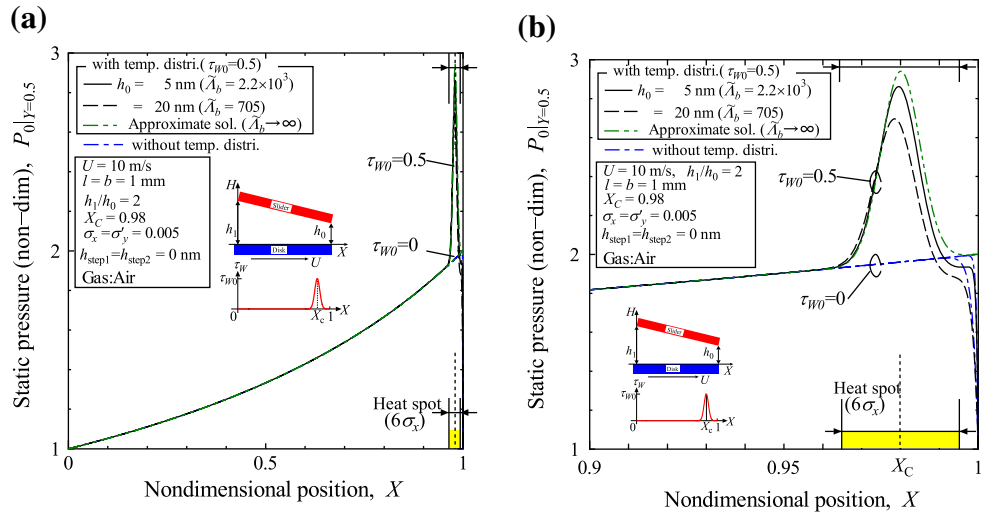


Fig. 5 Contour plots of additional static pressure produced by the heat spot for different spacings (in air). **a** $h_0 = 5$ nm ($\Lambda_b = 2.2 \times 10^3$, $\delta P_{OHT} = 1$), **b** $h_0 = 20$ nm ($\Lambda_b = 705$, $\delta P_{OHT} = 1$)

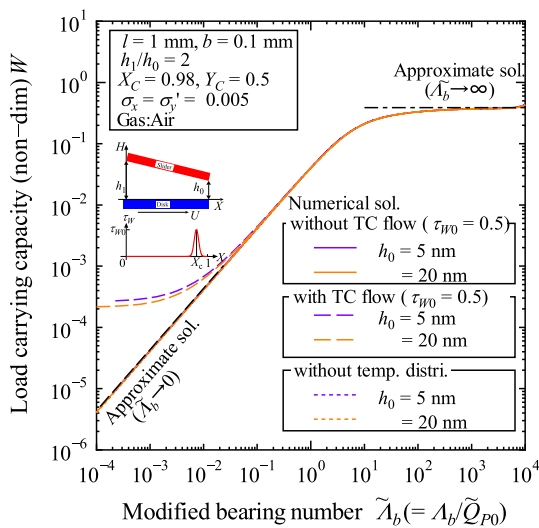


Fig. 6 Load carrying capacity W vs. modified bearing number $\tilde{\Lambda}_b$ ($bl = 0.1$)

atmosphere with a Gaussian heat spot near the trailing edge with a minimum spacing of $h_0 = 5$ nm, that corresponds to Fig. 3. Moreover, in Fig. 7, a dynamic pressure spike can be observed near the trailing edge produced by the heat spot. Figure 8a, b show the translational stiffness distributions along the centerline ($Y = 0.5$) with the maximum temperature τ_{W0} as a parameter and minimum spacings of $h_0 = 5$ and 20 nm. Figure 8a shows a general view for $X = 0-1$, and Fig. 8b shows an enlarged view for $X = 0.9-1$. For smaller spacings, the pressure distributions approximately coincide with the approximate solutions for $\Lambda_b \rightarrow \infty$ (see Eq. (20)) corresponding to each maximum temperature τ_{W0} .

Figure 9 shows the translational stiffness contour plots in an air atmosphere with a Gaussian heat spot near the trailing edge with minimum spacings of $h_0 = 5$ and 20 nm and the corresponding modified bearing numbers of $\Lambda_b = 2.2 \times 10^3$ and 705, respectively. The stiffness contours for $h_0 = 5$ and 20 nm are approximately the same. Since the modified bearing number $\tilde{\Lambda}_b$ is very large for $h_0 = 5$ nm, the

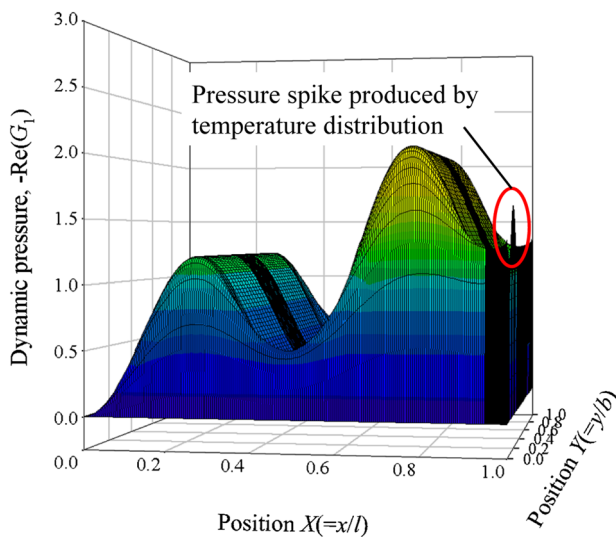


Fig. 7 Translational stiffness component $\{-\text{Re}(G_1)\}$ with temperature distribution (in air). $h_0 = 5 \text{ nm}$, $U = 10 \text{ m/s}$ ($\tilde{\Lambda}_b = 2.2 \times 10^3$), $h_1/h_0 = 2$, $h_{\text{step1}} = h_{\text{step2}} = 0$. Gas: Air, $\Omega = ff_0 = 1$, $\tau_{w0} = 0.5$

non-dimensional value of the pressure peak for $h_0 = 5 \text{ nm}$ is 0.55, which is comparable to the value of $\Delta G_{1HT}(=1)$, where ΔG_{1HT} denotes the theoretical maximum value of the additional pressure given by Eq. (30) (see “Appendix 1”).

Figure 10a shows the relationships between translational stiffness, κ_{11} , and frequency ratio, $\Omega(=ff_0)$, and Fig. 10b shows the relationships between the translational damping coefficient, $\Omega\gamma_{11}$, and the frequency ratio, Ω , with minimum spacing h_0 as a parameter. The definitions of stiffness, κ_{ij} , and damping coefficients, $\Omega\gamma_{ij}$, are shown in “Appendix 2”. The tendency for $h_0 = 20$ and 5 nm and the infinite bearing number solution ($\Lambda_b \rightarrow \infty$) are approximately the same.

Figure 11 shows the relationships between the translational stiffness, κ_{11} , and the modified bearing number $\tilde{\Lambda}_b (= \Lambda_b/\tilde{Q}P_0)$. For very large $\tilde{\Lambda}_b$, κ_{11} is approximately

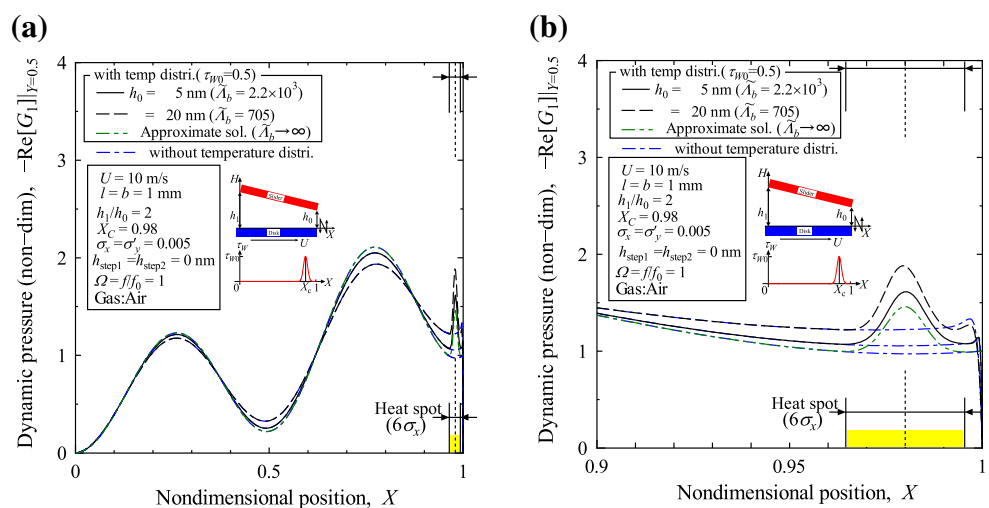
constant and coincides with the approximate value for $\tilde{\Lambda}_b \rightarrow \infty$ (Eq. (20)). For $10^{-2} < \tilde{\Lambda}_b < 10^2$, κ_{11} decreases and approaches the incompressible short bearing approximation ($\tilde{\Lambda}_b \rightarrow 0$, Eq. (26)), which is proportional to $\tilde{\Lambda}_b$. For $\tilde{\Lambda}_b < 10^{-2}$, the numerical solutions approach constant values, whereas the short bearing approximation ($\tilde{\Lambda}_b \rightarrow 0$) continues to decrease. These differences between the numerical solutions and the short bearing approximation occur because numerical solutions for κ_{ij} that include the thermal creep flow term yield dynamic pressures produced by the thermal-wedge effect. [Note that in the short bearing approximation equation ($\tilde{\Lambda}_b \rightarrow 0$), the thermal creep flow term vanishes automatically.]

5.3 Flying characteristics analysis of a step slider with the TFC effect (Case 2)

Next, we used a slider having steps of two different depths (five-pad negative-pressure slider) with a length l of 1.25 mm, a width b of 1 mm, and step depths h_{step1} and h_{step2} of 0.35 and 3 μm , respectively. In addition, the slider is equipped with an embedded heater at the end, as shown in Fig. 12a. When the heater is powered off (heater off), the pressure generated by MGL effects and vdW attractive pressure acts on the slider. On the other hand, when the heater is powered on (heater on), the flying height is finally reduced by the effect of additional repulsive t-MGL pressure and vdW attractive pressure, due to the temperature distribution and the thermal deformation.

The temperature distribution at the slider surface is considered to be Gaussian with a non-dimensional maximum temperature τ_{w0} of 0.1 and a maximum thermal deformation (projection) d_{max} of 5.5 nm, as shown in Fig. 12a (standard deviation $\sigma_x = \sigma_y = 0.005$, center of distribution $X_C = 0.98$, $Y_C = 0.5$). The essential parameter for estimating the pressure generation is the modified bearing number

Fig. 8 Translational stiffness component $\{-\text{Re}(G_1)\}$ for different spacings (in air). **a** General view ($X = 0-1$), **b** enlarged view ($X = 0.9-1$)



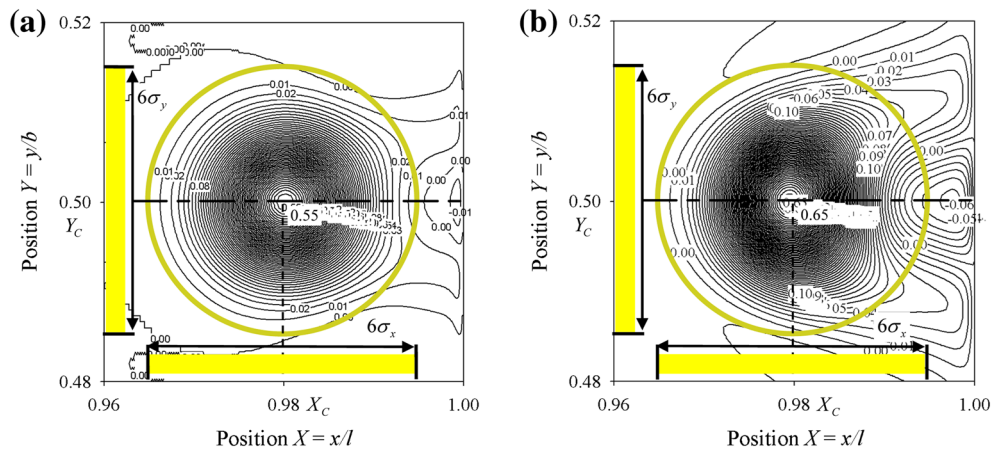


Fig. 9 Contour plots of additional dynamic pressure $\{-\text{Re}(G_i)\}$ produced by the heat spot for different spacings (in air), $\tau_{w0} = 0.5$. **a** $h_0 = 5$ nm ($\tilde{A}_b = 2.2 \times 10^3$, $Q_{TP} = 0.356$, $-\text{Re}[G_{1HT}] = 0.5$), **b** $h_0 = 20$ nm ($\tilde{A}_b = 705$, $Q_{TP} = 0.290$, $-\text{Re}[G_{1HT}] = 0.5$)

Fig. 10 Translational stiffness and damping coefficient for different spacings (in air), $\tau_{w0} = 0.5$. **a** Translational stiffness, **b** translational damping coefficient

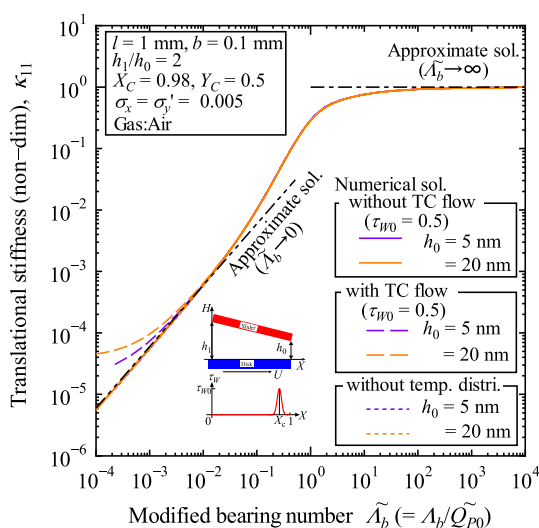
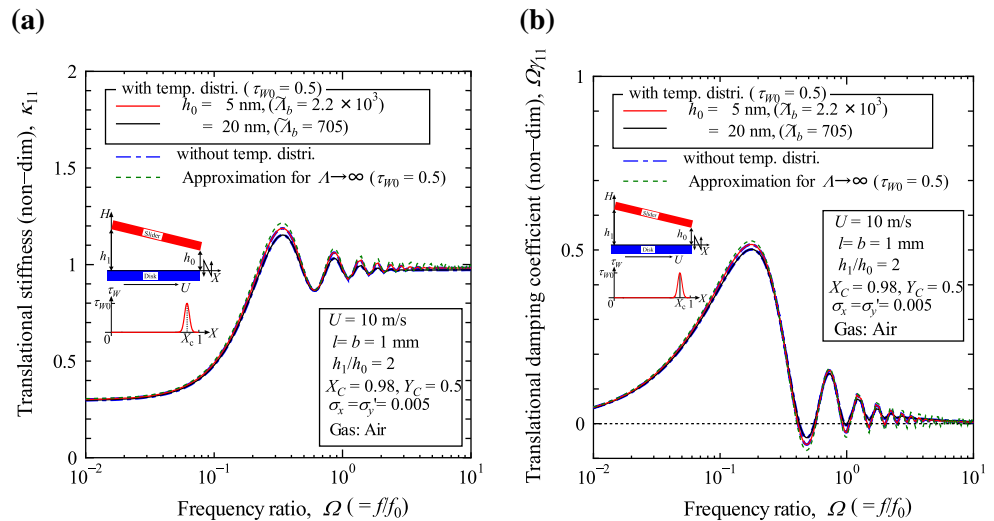


Fig. 11 Translational stiffness vs. modified bearing number \tilde{A}_b for different spacings (in air) ($b/l = 0.1$)

$\tilde{A}_b = (b/l)^2 \cdot \Lambda / \tilde{Q}_{P0}$ (Fukui et al. 1996), where \tilde{Q}_{P0} is the pressure flow rate ratio in the reference state.

5.3.1 Static flying characteristics

Figure 13 shows the flying heights, h_0 and h_{\min} , for a load of $w = 9.8$ mN and a pressure center of $\bar{X} = 0.5$ as a function of the disk velocity U . Here, h_0 and h_{\min} are, respectively, the spacing at the trailing edge and the minimum spacing with heating, as shown in Fig. 12a. The flying characteristics are examined for the following conditions: (a) with and without laser heating (heater on/off), (b) with and without van der Waals pressure, and (c) in air and He.

Table 1 gives the static flying states (h_0 or h_{\min} and the inclination of the slider h_1/h_0) of Fig. 13 for $U = 30$ m/s. Even if we consider the pressure generated by the thermal deformation and the increase in the vdW attractive force, the minimum spacing h_{\min} is smaller than the case without heating by

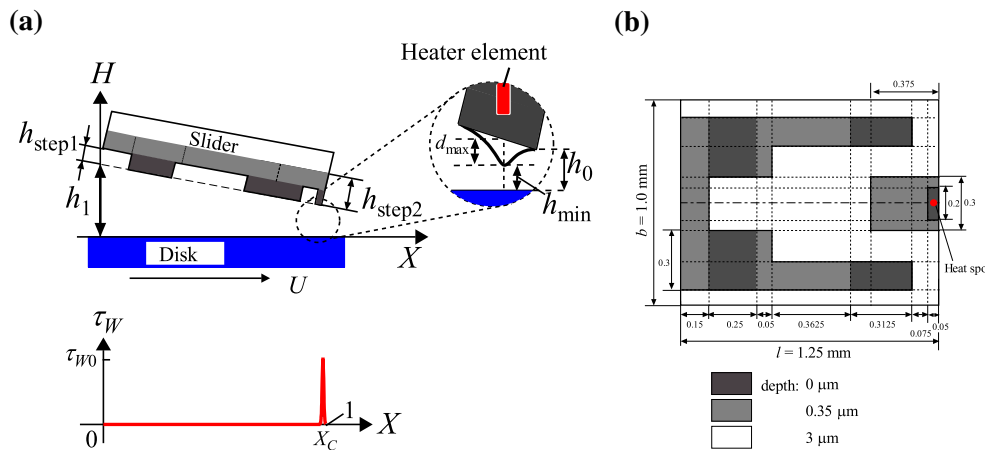


Fig. 12 Two-step-depth-type slider with thermal flying height (TFC) effect (Case 2) (negative-pressure-type, five-pad slider). **a** Side view, **b** bottom view

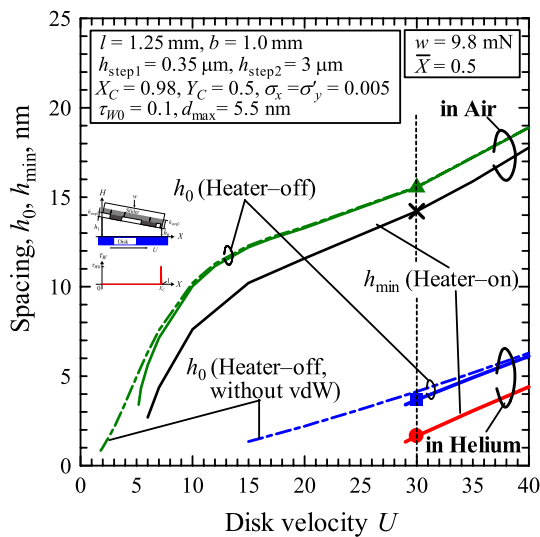


Fig. 13 Spacings h_0 and h_{min} vs. disk speed U (heater on/off, $\tau_{W0} = 0.1$, in air/He)

the heater, because the slider surface is protruded by the effect of heating ($d_{max} = 5.5$ nm). When the ambient gas is He, the slider inclination h_1/h_0 is larger than in the case with air.

Figure 14a, b show the static pressure for the flying state of Fig. 13 with heating by the heater for $U = 30$ m/s. Figure 14a shows the static pressure in air corresponding to the symbol, \times , and Fig. 14b shows that in He corresponding to the symbol, \bullet in red. A pressure spike occurs in the applied temperature area by the effect of heating. Figure 15a, b show the pressure distributions along the centerline ($Y = 0.5$) with and without the temperature distributions (heater on/off) and in air and He, respectively. Figure 15a shows a general view for $X = 0-1$, and Fig. 15b shows an enlarged view for $X = 0.9-1$.

5.3.2 Dynamic flying characteristics

Figure 16a, b show the translational stiffness components $\{-Re(G_1)\}$ for the flying state of the frequency ratio $\Omega = 1$

Table 1 Static flying states for ambient gas (air/He) and heater condition (heater-on/off, $\tau_{W0} = 0.1$)

Heater	Effects		Air	Helium
on	<ul style="list-style-type: none"> t-MGL pressure Thermal distribution Slider projection vdW pressure 	h_{min} (nm)	14.21	1.65
		h_1/h_0	13.97	40.85
off	<ul style="list-style-type: none"> MGL pressure vdW pressure 	h_0 (nm)	15.54	3.68
		h_1/h_0	14.14	44.61
	<ul style="list-style-type: none"> MGL pressure 	h_0 (nm)	15.58	4.13
h_1/h_0		14.11	39.58	

(Flying condition: $w=9.8$ mN, $\bar{X}=0.5$, $U=30$ m/s)

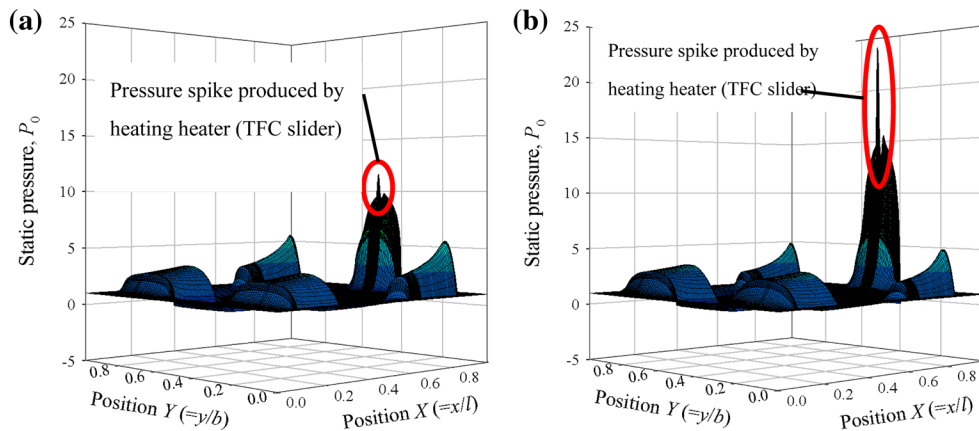


Fig. 14 Static pressure distributions corresponding to symbols, *times symbol* and *filled circle* in Fig. 13 and Table 1 (heater-on, $\tau_{W0} = 0.1$, in air/He, $U = 30$ m/s). **a** In air ($h_{\min} = 14.21$ nm, $h_1/h_0 = 13.97$,

symbol *times symbol*). **b** In helium ($h_{\min} = 1.65$ nm, $h_1/h_0 = 40.85$, symbol *filled circle*) (color figure online)

Fig. 15 Cross section ($Y = 0.5$) of static pressure distributions corresponding to symbols, *times symbol*, *filled circle*, *filled triangle*, and *filled square* (heater-on/off, $\tau_{W0} = 0.1$, in air/He, $U = 30$ m/s). **a** General view ($X = 0-1$), **b** enlarged view ($X = 0.9-1$)

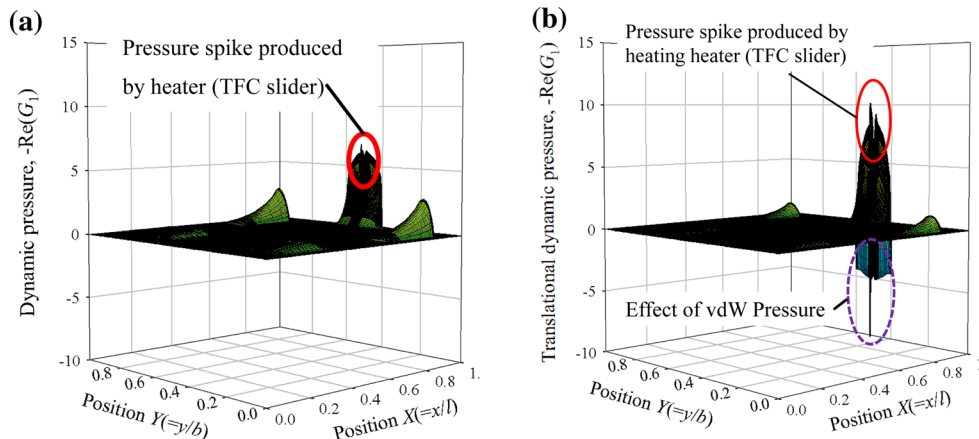
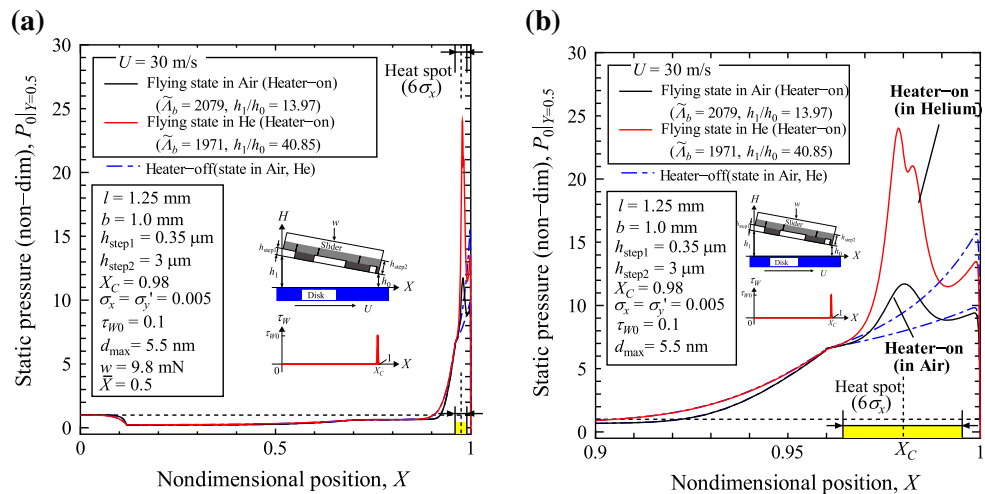


Fig. 16 Translational stiffness components $\{-\text{Re}(G_1)\}$ corresponding to symbols, *times symbol* and *filled circle* (heater-on, $\tau_{W0} = 0.1$, in air/helium, $U = 30$ m/s, $\Omega = 1$). **a** In air ($h_{\min} = 14.21$ nm,

$h_1/h_0 = 13.97$, symbol *times symbol*). **b** In helium ($h_{\min} = 1.65$ nm, $h_1/h_0 = 40.85$, symbol *filled square*)

Fig. 17 Cross section ($Y = 0.5$) of translational stiffness distributions $\{-\text{Re}(G_1)\}$ corresponding to symbols, *times symbol*, *filled circle*, *filled triangle*, and *filled square* (heater on/off, $\tau_{w0} = 0.1$, in air/He, $U = 30$ m/s, $\Omega = 1$). **a** General view ($X = 0-1$), **b** enlarged view ($X = 0.9-1$)

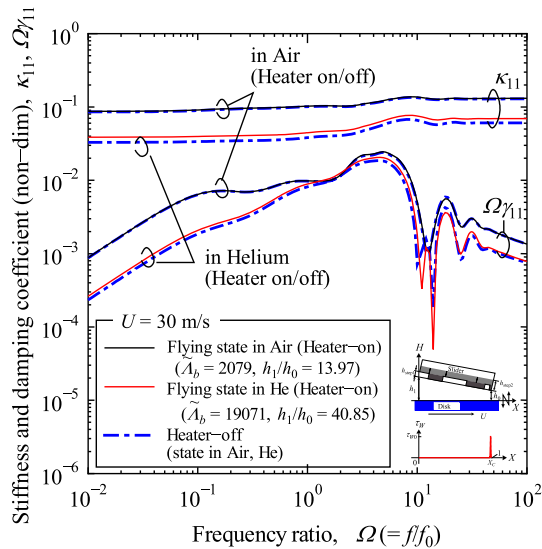
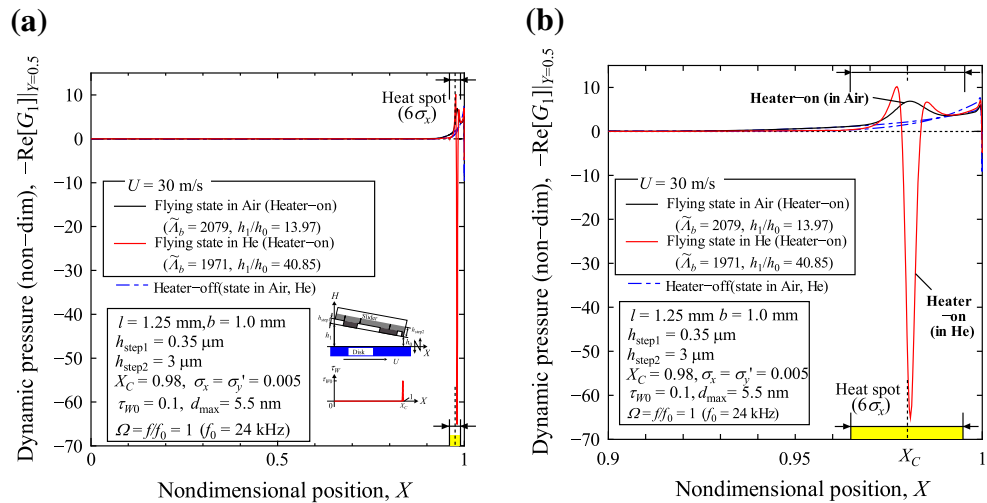


Fig. 18 Stiffnesses and damping coefficients corresponding to symbols, *times symbol*, *filled circle*, *filled triangle*, and *filled square* (heater on/off, $\tau_{w0} = 0.1$, in air/He, $U = 30$ m/s)

($f = f_0 = 24$ kHz) shown in Fig. 14a, b. Figure 17a, b show the translational stiffness distributions along the centerline ($Y = 0.5$) with and without temperature distributions (heater on/off) and in air and Helium. Figure 17a shows a general view for $X = 0-1$, and Fig. 17b shows an enlarged view for $X = 0.9-1$. A pressure spike also occurs in the dynamic pressure coefficient as a result of heating as well as the static pressure in Fig. 14a, b. Moreover, the effect of the vdW attractive force is remarkable because the minimum spacing decreases locally as a result of thermal deformation due to heating by the heater.

Figure 18 shows the relationships between the translational stiffness, κ_{11} , the translational damping coefficient, $\Omega\gamma_{11}$, which are integral values of the dynamic pressure

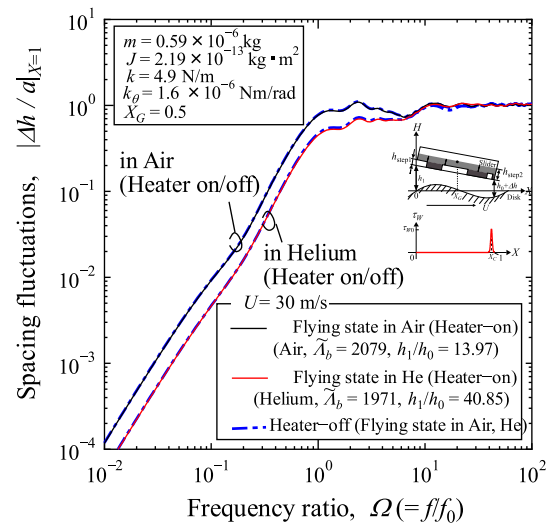


Fig. 19 Spacing fluctuations corresponding to symbols, *times symbol*, *filled circle*, *filled triangle*, and *filled square* (heater on/off, $\tau_{w0} = 0.1$, in air/He, $U = 30$ m/s)

coefficient, G_1 , and the frequency ratio, Ω . The curves in Fig. 18 correspond to the symbols \times , \bullet , \blacktriangle , and \blacksquare in Fig. 13 and Table 1. When the ambient gas is replaced with He, Fig. 18 shows that κ_{11} and $\Omega\gamma_{11}$ decrease compared with the case of air. Figure 19 shows the relationships between the spacing fluctuation ratio $|\Delta h/a|$ and the frequency ratio Ω (Fukui et al. 1985). By replacing the ambient gas with He, the spacing fluctuation ratio at the trailing edge ($X = 1$) is reduced compared with the case in air because the inlet-to-outlet spacing ratio (h_1/h_0) increases. In this calculation condition, the influence of the heating on the translational stiffness, κ_{11} , the translational damping coefficient, $\Omega\gamma_{11}$, and the spacing fluctuation ratio, $|\Delta h/a|$, is negligible.

6 Conclusion

In the present paper, the characteristics of a plane inclined slider (Case 1) and a step slider flying in either air or He (Case 2) over a running boundary wall with local temperature distributions are analyzed using the thermo-molecular gas-film lubrication (t-MGL) equation. For a plane inclined slider (Case 1), the fundamental static and dynamic characteristics are analyzed numerically and are examined through two limiting approximations: the approximation for infinite bearing number and the incompressible short bearing approximation. For a step slider (Case 2), the decreases in the minimum spacing for a slider flying in He are significant because the mean free path of He, λ_{He} , is approximately three times that of air, λ_{air} . The increases in the minimum spacing due to laser heating are negligible in both air and He because the heat spot size is very small. Moreover, the decrease in the minimum spacing produced by thermal deformation (projection height, d_{max}) by laser heating in the thermal fly-height control (TFC) slider is reduced by the total additional pressure of (1) MGL pressures produced by the air-film wedge effect, (2) t-MGL pressures produced by the applied temperature distribution, and (3) van der Waals attractive pressure due to the ultra-small spacing. The spacing fluctuation in He caused by a running wavy disk is smaller than that in air, because the inlet-to-outlet spacing ratio (h_1/h_0) in He is larger than that in air.

Appendix 1: Theoretical maximum pressure increase produced by boundary temperature

For a plane inclined slider with a minimum spacing of several nanometers, the pressure increase produced by the boundary temperature distribution can be estimated using the following index. In this estimation, the heat spot is considered to be approximately the same as the minimum spacing point on the centerline.

For a static pressure increase:

$$\begin{aligned} \delta P_{OHT} &\equiv \{P_{0\tau_W} - P_0|_{\tau_W=0}\}_{X=X_C, Y=Y_C} \\ &\cong \{P_{0\tau_W} - P_0|_{\tau_W=0}\}_{X=1, Y=Y_C} \quad (\text{for } Y_C = 0.5) \\ &= H'_1 \cdot \tau_{W0}. \end{aligned} \quad (29)$$

For a dynamic pressure increase:

$$\begin{aligned} \delta G_{1HT} &\equiv \{G_{1\tau_W} - G_1|_{\tau_W=0}\}_{X=X_C, Y=Y_C} \\ &\cong \{G_{1\tau_W} - G_1|_{\tau_W=0}\}_{X=1, Y=Y_C} \quad (\text{for } Y_C = 0.5) \\ &= \tau_{W0} \cdot [\{\cos(4\pi\Omega) - H'_1\} - i \cdot \sin(4\pi\Omega)] \end{aligned} \quad (30)$$

$$\begin{aligned} \delta G_{2HT} &\equiv \{G_{2\tau_W} - G_2|_{\tau_W=0}\}_{X=X_C, Y=Y_C} \\ &\cong \{G_{2\tau_W} - G_2|_{\tau_W=0}\}_{X=1, Y=Y_C} \quad (\text{for } Y_C = 0.5) \\ &= \tau_{W0} \cdot [\{X_G \cos(4\pi\Omega) - H'_1(X_G - 1)\} - i \cdot X_G \sin(4\pi\Omega)] \end{aligned} \quad (31)$$

$$\begin{aligned} \delta G_{3HT} &\equiv \{G_{3\tau_W} - G_3|_{\tau_W=0}\}_{X=X_C, Y=Y_C} \\ &\cong \{G_{3\tau_W} - G_3|_{\tau_W=0}\}_{X=1, Y=Y_C} \quad (\text{for } Y_C = 0.5) \\ &= \tau_{W0} \cdot [\{\cos(4\pi\Omega) - H'_1 \cos(2\pi\Omega)\} \\ &\quad - i \cdot \{\sin(4\pi\Omega) - H'_1 \sin(2\pi\Omega)\}]. \end{aligned} \quad (32)$$

Appendix 2: Definitions of stiffness, κ_{ij} , and damping coefficients, $\Omega\gamma_{ij}$

$$\begin{aligned} \kappa_{1j} &= - \int_0^1 \int_0^1 \text{Re}(G_j) dXdY, \\ \kappa_{2j} &= - \int_0^1 \int_0^1 \text{Re}(G_j) \cdot (X_G - X) dXdY \\ \Omega\gamma_{1j} &= - \int_0^1 \int_0^1 \text{Im}(G_j) dXdY, \\ \Omega\gamma_{2j} &= - \int_0^1 \int_0^1 \text{Im}(G_j) \cdot (X_G - X) dXdY \quad \text{for } j = 1 \text{ and } 2. \end{aligned} \quad (33)$$

References

- Dahl JB, Bogy DB (2014) Static and dynamic slider air-bearing behavior in heat-assisted magnetic recording under thermal flying height control and laser system-induced protrusion. *Tribol Lett* 54(1):35–50
- Fukui S, Kaneko R (1988) Analysis of ultra-thin gas film lubrication based on linearized Boltzmann equation: first report-derivation of a generalized lubrication equation including thermal creep flow. *Trans ASME J Tribol* 110:253–262
- Fukui S, Kaneko R (1990a) Dynamic analysis of flying head sliders with ultra-thin spacing based on the Boltzmann equation (comparison with two limiting approximations). *JSME Int J Ser III* 33(1):76–82
- Fukui S, Kaneko R (1990b) A database for interpolation of Poiseuille flow rates for high Knudsen number lubrication problems. *ASME J Tribol* 112(1):78–83
- Fukui S, Kogure K, Mitsuya Y (1985) Dynamic characteristics of flying-head sliders on running wavy disk. *ASLE SP-19*:52–58
- Fukui S, Matsuda R, Kaneko R (1996) On the physical meanings of and in molecular gas film lubrication problems. *Trans ASME* 118:364–369
- Fukui S, Yamane K, Matsuoka H (2001) Novel laser-assisted micro levitation mechanism for magneto-optical recording. *IEEE Trans Magn* 37:1845–1848
- Fukui S, Kitagawa N, Wakabayashi R, Yamane K, Matsuoka H (2014a) Thermo-molecular gas-film lubrication (t-MGL) analysis for heat-assisted magnetic recording head sliders. *Microsyst Technol* 20:1447–1454
- Fukui S, Wakabayashi R, Matsuoka H (2014b) Static flying characteristics of heat-assisted magnetic recording heads in He-enclosed HDDs. *IEEE Trans Mag* 50(11). doi:10.1109/TMAG.2014.2320961

- Israelachivili JN (1992) *Intermolecular and surface forces*, 2nd edn. Academic Press, New York
- Kurita M, Xu J, Tokuyama M, Nakamoto K, Saegusa S, Maruyama Y (2005) Flying-height reduction of magnetic-head slider due to thermal protrusion. *IEEE Trans Magn* 41(1):3007–3009
- Liu N, Zheng JJ, Bogy DB (2011) Thermal flying-height control sliders in air-helium gas mixtures. *IEEE Trans Magn* 47(1):100–104
- Matsuoka H, Ohkubo S, Fukui S (2005) Corrected expression of the van der Waals pressure for multilayered system with application to analysis of static characteristics of flying head sliders with an ultrasmall spacing. *Microsyst Technol* 11:824–829
- Ohkubo T, Fukui S, Kogure K (1989) Static characteristics of gas-lubricated slider bearings operating in a helium–air mixture. *Trans ASME J Tribol* 111(4):620–627
- Ono K (1975) Dynamic characteristics of air-lubricated slider bearing for noncontact magnetic recording. *Trans ASME Ser F J Lubr Tech* 97-2:250–258
- Peng W, Hsia Y, Sendur K, McDaniel T (2005) Thermo-magneto-mechanical analysis of head-disk interface in heat assisted magnetic recording. *Tribol Int* 38(1):588–593